Laser plasma interactions in fused silica cavities

Xianzhong Zeng, Xianglei Mao, Samuel S. Mao, Jong H. Yoo, Ralph Greif, Richard E. Russo*

Lawrence Berkeley National Laboratory, Berkeley, CA 94720

*corresponding author

Abstract

The effect of laser energy on formation of a plasma inside a cavity was investigated. The temperature and electron number density of laser-induced plasmas in a fused silica cavity were determined using spectroscopic methods, and compared with laser ablation on a flat surface. Plasma temperature and electron number density during laser ablation in a cavity with aspect ratio of 4 increased faster with irradiance after the laser irradiance reached a threshold of 5 GW/cm^2. The threshold irradiance of particulate ejection was lower for laser ablation in a cavity compared with on a flat surface; the greater the cavity aspect ratio, the lower the threshold irradiance. The ionization of silicon becomes saturated and the crater depths were increased approximately by an order of magnitude after the irradiance reached the threshold. Phase explosion was discussed to explain the large change of both plasma characteristics and mass removal when irradiance increased beyond a threshold value. Self-focusing of the laser beam was discussed to be responsible for the decrease of the threshold in cavities.

Keywords: Laser ablation, Cavity structure, Laser-induced plasma

1. Introduction

Many laser–material interaction processes produce cavity structures; e.g. laser drilling, micromachining, and depth resolved chemical analysis [1, 2, 3]. Elemental depth variations in solid samples are important for micro analytical applications, e.g., analysis of spatial heterogeneity of inclusions. Previous studies [4, 5, 6] showed that the cavity aspect ratio influenced elemental fractionation, a process during which elements are selectively ablated; the ablated mass composition changes as the cavity forms even for homogeneous samples. Mechanisms to describe the effect of the cavity on fractionation have not been established. One possible mechanism is that low melting/vaporization point elements are preferentially removed due to higher plasma temperature inside a cavity [4, 7]. The laser induced plasma in a cavity was found to have a larger electron number density and to be at a higher temperature compared to a plasma produced on a flat surface. The greater the cavity depth to diameter ratio (aspect ratio), the greater was the plasma temperature and electron number density inside the cavity [7].

The amount of laser energy absorbed by a material influences the amount of mass removed, its temperature, phase, and degree of ionization in the plasma [8]. Laser beam energy coupling to a solid was found to increase as a cavity was formed in a target [9, 10]. The increase in energy coupling was related to the cavity depth-to-diameter (aspect) ratio. Shannon's [9] radiative-cavity analysis demonstrated that energy coupling in a cavity increased with increasing aspect ratio. For an aspect ratio varying from 0 to 5, the amount of energy coupled increased approx 10 times compared to the energy coupled to a flat surface. Jeong, et al. [10] reported an increase in coupled laser-beam energy by

multiple-reflections of the cavity walls, utilizing a photothermal deflection technique to measure the refractive index change of the ambient medium adjacent to the sample.

The influence of crater formation on the plasma characteristics at different laser energy levels remains unexplored. With increasing laser irradiance, a dramatic change in the plasma characteristics and a sharp increase of mass removal were observed using high power nanosecond lasers and silicon samples [11, 12]. The threshold irradiance was about 20 GW/cm^2. Explosive boiling was proposed to explain these changes. Since energy coupling and plasma properties are related to the cavity aspect ratio, it is of interest to study how the threshold irradiance of explosive boiling is influenced by the cavity aspect ratio.

In this work, plasma properties were measured at different laser irradiances for laser ablation in fused silica cavities with different aspect ratios and compared to flat surface data. The irradiance range was 2 – 40 GW/cm^2. The spatial distribution (from the bottom of the cavity to a height 1 mm above the target surface) of the plasma temperature and electron number density were determined by measuring the Stark broadening of the Si emission lines and the relative line-continuum ratio at a time of 30 ns after the laser pulse.

2. Experimental system

A diagram of the experimental system can be found in ref. [11]. A 266 nm Nd:YAG laser (Coherent, Infinity) with a 3-ns pulse-width was used as the ablation laser. The laser

beam was focused onto the sample with a quartz lens to a spot diameter of ~50 microns. The ambient above the sample was air at 1 atm. pressure. The pulse energy was measured using a pyroelectric detector and a joulemeter. A second lens was used to image the laser-induced plasma onto the entrance slit of a Czerny-Turner spectrometer (Spex Industries Model 270M). Spectral emission was detected by an Intensified Charge-Coupled Device (ICCD) system which consisted of a thermoelectrically cooled CCD (EG&G Princeton Applied Research Model OMA VISION) with 512×512 pixels and a Microchannel Plate (MCP) image intensifier. This detection system provided a spectral window of ~13 nm and resolution of typically 0.125 nm, using an entrance slit width of 20 micron and grating with 1800 grooves/mm. The spatial resolution of the ICCD spectrometer plus lens arrangements was 11 microns per pixel. The dark current background of the ICCD detector was subtracted from the measured spectroscopic data for each measurement.

Gating the ICCD and changing the delay time enabled the spectra to be temporally resolved. The gate width and time delay were controlled by the OMA SPEC 4000 software (EG&G Princeton Applied Research), and synchronously triggered from the Nd:YAG laser. The gate width was set at 30 ns. A photo diode and a digitizing oscilloscope were used to calibrate the time delay. The delay time was fixed at 30 ns. At delay times less than 30 ns, only continuum emission was observed.

Fused silica was cut into samples of 2 mm width and 2 mm height, and placed on an *xyz* translation stage. Cavities were pre-fabricated using Gaussian beam nanosecond laser ablation, by varying the lens-to-sample distance (spot size), energy, and number of

pulses. Two cavities with the same depth of about 0.5 mm, but different diameters (130 micron, 250 micron) were fabricated with aspect ratios of 2 and 4. A white-light interferometric microscope (New View 200, Zygo Corporation) and CCD camera system were used to measure the exact cavity dimensions. Single pulse laser ablation at different laser energies was subsequently performed at the bottom surface of the cavities. The silicon emission line Si(I) at 288.16 nm was measured for diagnosing plasma properties (plasma temperature and electron number density). The plasma properties were measured in the cavities (spectra were obtained from emission passing through the transparent cavity walls) and were compared to those from ablation at the flat sample. The spot size (fluence) was equal when the laser beam was incident on the flat surface and on the bottom surface of each cavity.

3. Results and discussion

A comparison of spectra from ablation inside a cavity versus a flat surface is shown in Fig. 1. The spectral lines were measured at a distance of 1 mm above the surface (either original flat surface or bottom of cavity), the peak position of plasma emission intensity. The line shape was found to best fit a Lorentzian function, indicating self-absorption was negligible. For ablation inside the cavity, the spectra had a wider Full Width at Half Maximum (FWHM) and greater emission intensity.

Plasma temperature

Under the assumption of local thermal equilibrium (LTE), the electron temperature T_e can be assumed equal to the excitation temperature T_{exc}, namely $T_e = T_{exc} = T$. Therefore, the

plasma temperature T can be determined by the line-to-continuum intensity ratio $\varepsilon_c/\varepsilon_l$, where ε_c is the continuum emission coefficient and ε_l is the integrated emission coefficient over the line spectral profile. In a previous study [7], only the first ionization potential of silicon was considered in the spectral analysis. However, as laser intensity and plasma temperature increases, higher ionization levels should be included.

The emission coefficient ε_l can be expressed in terms of the electron temperature and density [13]:

$$\varepsilon_l = \left(\frac{h\nu}{4\pi}\right) A_{21} \frac{g_2}{2Z_{ion}(T)} \frac{h^3}{(2\pi mk)^{3/2}} n_e n_i T_e^{-3/2} \exp\left(\frac{E_{ion} - E_2 - \Delta E_i}{kT_e}\right), \quad (1)$$

where A_{21} is the Einstein transition probability of spontaneous emission, and E_{ion} is the ionization potential. E_2 and g_2 are upper level energy and degeneracy, respectively. ΔE_i is the lowering of the ionization potential of atoms in the presence of a field of ions and is small enough to be neglected. $Z_{ion}(T)$ is the partition function for ions, which is given by [14]:

$$Z_{ion}(T) = \sum_i g_i \exp\left(-\frac{E_i}{kT}\right), \quad (2)$$

with g_i the degeneracy or statistical weight of the i-th energy level E_i,

$$g_i = 2J_i + 1, \quad (3)$$

where J_i is the angular momentum quantum number of the level. The values of E_i and J_i were obtained from the NIST data bank [15]. The partition functions of silicon atoms, singly-charged and doubly-charged silicon ions were calculated for the temperature interval from 6,000 to 50,000 K. The data were fit with third-, fourth-, and fifth-order polynomials using a least squares method. Each of these fits was then compared to the

original data at temperatures of 6000, 25000 and 50000 K. The fifth-order polynomials were selected due to the lowest total error.

$$Z(T) = a + b\mathrm{Y} + c\mathrm{Y}^2 + d\mathrm{Y}^3 + e\mathrm{Y}^4 + f\mathrm{Y}^5, \quad (4)$$

where $Y = T \times 10^{-4}$ K; a, b, c, d, e and f are given in Table I. The calculated values of the partition function agree with those reported in ref. 16 to within 0.5% for temperatures between 6000 and 12000 K (the largest temperature range available in the literature).

Based on the calculations using Saha equation, and the electron number density measured in this work, the first ionization level of silicon is dominant for temperatures less than 25000 K. For greater temperatures, the ionization shifts toward higher levels. The doubly charged silicon ions are dominant when the temperature is greater than 40000 K.

By including the second ionization contribution to the continuum radiation, the continuum emission coefficient can be rewritten as [13, 14]:

$$\varepsilon_c = \left(\frac{16\pi e^6}{3c^3\left(6\pi m^3 k\right)^{1/2}}\right) n_e (n_i^+ + 4n_i^{++}) T_e^{-1/2} \left[\xi\left(1 - \exp\frac{-h\nu}{kT_e}\right) + G\left(\exp\frac{-h\nu}{kT_e}\right)\right]. \quad (5)$$

From equations (1) and (5), the line to continuum ratio is:

$$\frac{\varepsilon_l}{\varepsilon_c} = \frac{1}{1 + 4\left(\frac{n_i^{2+}}{n_i^+}\right)} C_r A_{21} \frac{g_2}{Z_{ion}} \frac{\lambda_c^2}{\lambda_l T_e} \frac{\exp\left(\frac{E_i - E_2 - \Delta E_i}{kT_e}\right)}{\left[\xi\left(1 - \exp\left(\frac{-hc}{\lambda k T_e}\right)\right) + G\left(\exp\left(\frac{-hc}{\lambda k T_e}\right)\right)\right]}, \quad (6)$$

where Z_{ion} is the partition function for ions. λ_c , λ_l are the continuum and center wavelength of the spectral line, respectively. The center wavelength position was obtained from the Lorentzian fit of the data. The ratio $\varepsilon_c / \varepsilon_l$ can be calculated from the

integrated line intensity and continuum intensity at λ_c and λ_l. The parameters used in Eq. (6) to determine T_e and n_e from the experimental data are listed in Table II [17, 18]. The ion ratio $\frac{n_i^{++}}{n_i^{+}}$ can be calculated from equation (7) in the following ion formation efficiency analysis.

The formation efficiencies of singly and doubly charged ions are calculated using the Saha equation [19]:

$$\frac{M^{++}}{M^{+}} = \frac{(2\pi m_e kT)^{3/2}}{h^3} \frac{2Z_M^{++}(T)}{Z_M^{+}(T)} \frac{1}{n_e} \exp\left(-\frac{E_{2,ion}}{kT}\right), \quad (7)$$

$$\frac{M^{+}}{M^{0}} = \frac{(2\pi m_e kT)^{3/2}}{h^3} \frac{2Z_M^{+}(T)}{Z_M^{0}(T)} \frac{1}{n_e} \exp\left(-\frac{E_{1,ion}}{kT}\right), \quad (8)$$

and the unit condition:

$$M^0 + M^+ + M^{++} = 1, \quad (9)$$

where m_e is the electron mass; h is the Planck constant; k is the Boltzmann constant; $Z_M^0(T)$, $Z_M^+(T)$ and $Z_M^{++}(T)$ are the partition functions at the temperature T for an atom, M^+ and M^{++} ions of an element M, respectively. $E_{1,\,ion}$ and $E_{2,\,ion}$ are the first and second ionization potentials, respectively.

In Eq. (6), the second ionization potential of Si is considered for calculating the plasma temperature. Based on the Saha equation, at higher plasma temperatures, ionization will shift towards even higher levels and electron collisions with the higher ionization states will contribute to continuum radiation. Thus, the temperature calculated from Eq. (6) may be greater than the actual plasma temperature.

Electron number densities

Stark line broadening from collisions of charged species is the primary mechanism influencing the emission spectra in these experiments. The FWHM of Stark broadened lines is related to the electron number density n_e by Eq. (10): [11]

$$\Delta\lambda_{1/2} = 2W\left(\frac{n_e}{10^{16}}\right)\left[1+1.75A\left(\frac{n_e}{10^{16}}\right)^{1/4}\left(1-\frac{3}{4}N_D^{-1/3}\right)\right], \qquad (10)$$

where N_D is the number of particles in the Debye sphere and is estimated from

$$N_D = 1.72\times10^{9}\frac{T^{3/2}}{n_e^{1/2}}. \qquad (11)$$

W is the electron impact parameter in nm and A is the ion impact parameter; W and A are functions of temperature and are approximated by second-order polynomials [17]:

$$W(T) = 4.8767\times10^{-4} + 1.6385\times10^{-8}\mathrm{T} - 1.8473\times10^{-13}T^2, \qquad (12)$$

$$A(T) = 0.03983 - 7.0226\times10^{-7}\mathrm{T} + 9.5699\times10^{-12}T^2. \qquad (13)$$

A Lorentz function was used to fit the spectra. The FWHM of Stark broadened lines and the line to continuum emission ratio were used to deduce the electron number density and temperature of the plasmas using equations 6 and 10.

The lower limit for the electron number density needed to collisionally maintain the energy-level populations to within 10% of LTE while competing with radiative decay is [11, 20, 21]:

$$n_e(cm^{-3}) \geq 1.4\times10^{14}(kT)^{1/2}\Delta E^3, \qquad (14)$$

where T is the temperature and ΔE is the energy difference between the upper and lower states. For the Si(I) transition at 288.16 nm, ΔE = 4.3 eV, and at the highest temperature kT = 4.9 eV, the lower limit for n_e is 2.5×10^{16} cm^{-3}, which is approximately two orders of magnitude lower than the value of n_e deduced from Stark broadening. Therefore, the validity of the LTE assumption is supported.

Effect of laser energy

Laser-sample and laser-plasma interactions are strongly dependent on the laser beam irradiance on the target. The plasma temperatures and electron number densities for laser ablation inside cavities and on a flat surface as a function of laser irradiance are shown in Figures 2a and 2b. The data were measured at a delay time 30 ns and at a distance of 1mm above the target. The electron number density and plasma temperature are greater at each irradiance as the cavity aspect ratio increases. For the flat surface, the electron number density and plasma temperature change dramatically at a threshold value of ~ 20 GW/cm^2. The threshold irradiance is lower for laser ablation in a fused silica cavity compared with a flat surface; the greater the cavity aspect ratio, the lower the threshold irradiance. For the aspect ratio of 2 cavity, the threshold value is ~ 9 GW/cm^2; for the aspect ratio of 4 cavity, the threshold value is ~ 5 GW/cm^2.

In the irradiance regions lower and higher than the threshold, the electron number density and plasma temperature increase faster with irradiance as the cavity aspect ratio increases (Figures 2a and 2b). These data are believed to be related to confinement and reflection effects by the cavity walls and plasma shielding. Once the plasma is generated in the

cavity, its lateral expansion is confined; electron number density increases greatly leading to enhanced absorption of the trailing part of the laser pulse. Additional electrons will be produced via electron-neutral, electron-ion inverse bremsstrahlung, and photoionization [22]. The absorbed energy is converted into internal energy of the plasma, resulting in a higher plasma temperature.

The spatial distributions of plasma temperature and electron number density for laser ablation inside a cavity and on a flat surface below and above the threshold irradiance at a time of 30 ns are shown in Figure 3. Below the threshold irradiance, the electron number densities do not change significantly with distance for both cavity and flat surface results (Fig. 3a and 3c). However, when the irradiances were greater than the threshold, the electron number densities exhibit a peak profile centered at about 0.5 mm from the surface. The maximum electron number density was about two times greater than the electron number densities below the threshold irradiance, while the irradiance increased only 23% for the flat surface results. For cavity results, the maximum electron number density was about three times greater with 50% increase of the irradiance. Plasma temperature also increased significantly after the threshold irradiances for both cavity and flat surface results (Fig. 3b and 3d). Due to heat transfer from the plasma to the cavity walls, plasma temperature decreases more rapidly as it expands from inside the cavity (Fig. 3d).

Fig. 4 shows the variation of the Si^+ and Si^{2+} formation efficiency versus laser irradiance. After the irradiance reaches the threshold, ionization becomes saturated for both the cavity and flat surface.

Once the plasma is initiated, absorption of laser radiation generally commences via electron-neutral inverse bermsstrahlung and photoionization of excited state atoms. However, when sufficient ionization is reached (>1%), the dominant laser absorption mechanism changes to electron-ion inverse bremsstrahlung, which involves the absorption of a photon by a free electron during electron-ion collisions [1, 11]. As shown in Fig. 4, the plasma is significantly ionized when the irradiance is greater than 1 GW/cm^2, ion density is much greater than the neutral atom density and the electron-ion inverse bremsstrahlung should dominate the absorption. The absorption coefficient $\alpha_p(cm^{-1})$ for electron-ion inverse bremsstrahlung can be written as [23]:

$$\alpha_p = (3.69\times10^8)\frac{Z^3 n_i^{\ 2}}{T^{1/2}\upsilon^3}\left[1-\exp(h\upsilon/kT)\right], \qquad (15)$$

where Z, n_i and T are, respectively, the average ion charge state, ion density, and temperature of the plasma.υ is the frequency of the laser light.

Assuming the plasma is in charge equilibrium, the average ion charge state and ion density are calculated from the electron number density and Si^+, Si^{++} formation efficiencies. Fig. 5 shows the calculated electron-ion inverse bremsstrahlung absorption coefficient vs. irradiance at a delay time of 30ns. For both cavity and flat surface, the absorption coefficient increased dramatically when the irradiance reached the threshold;

e.g., for the flat surface a value of about four times greater than the absorption coefficient below the threshold irradiance.

Besides inverse bremsstrahlung, other mechanisms including photoionization, impact ionization and thermal ionization, may affect the absorption of the plasma [24]. The laser irradiance absorbed by the plasma can be expressed as [1, 23]:

$$\Phi_{absorb} = \Phi(1 - \exp(-\alpha_p l)), \qquad (16)$$

where l is the physical thickness and $\alpha_p l$ is the optical thickness of the plasma. The absorbed energy is converted into internal energy of the plasma. With increasing irradiance, the temperature and the degree of ionization of the vapor increase, which leads to additional plasma absorption.

Fig. 6 shows crater depth changes with irradiance for laser ablation on the flat surface. The crater depth increased dramatically at the irradiance of ~20 GW/cm^2. As the irradiance was increased from 18 GW/cm^2 to 21 GW/cm^2, the crater depth abruptly increased from 1 to 10 μm per pulse. Fig. 7 shows the images of ejected mass obtained by femtosecond laser shadowgraphy for laser irradiances below and above the threshold value, at time of 2 μs after the laser pulse. At an irradiance slightly higher than threshold (Fig. 7a), the image clearly shows the ejection of particulates in the size of several tens of microns. However, ejection of particulates was not detected for irradiances lower than threshold (Fig. 7b). These data are consistent with the explosive boiling (phase explosion) study by J. H. Yoo, et al. [12].

A possible mechanism for the large change of both plasma characteristics and mass removal when irradiance increases beyond a threshold is explosive boiling [25, 26]. Explosive boiling occurs when the sample is heated rapidly and the molten layer becomes superheated. Superheated liquid near the critical state experiences large density fluctuations. In the superheated liquid, these fluctuations can generate vapor bubbles. When vapor bubbles reach a critical radius, they expand spontaneously. The rapid expansion of these vapor bubbles in the superheated liquid leads to the ejection of particulates [12].

One possible explanation for the decrease of the threshold value in the cavity is self-focusing of the laser beam due to density gradient in the plasma. Hora [27] derived the laser power threshold for nonlinear-force self-focusing of a laser beam in a plasma:

$$P \geq \begin{cases} 1.46\times10^{6}T^{-5/4} & for \quad \omega_p \leq \omega \quad and \quad T \geq 10ev \\ 1.15\times10^{4}T & for \quad \omega_p << \omega \end{cases}, \qquad (17)$$

where P is laser power in watts, T is plasma temperature in eV, ω_p is the plasma frequency, $\omega_p = 8.9\times10^{3}\cdot\sqrt{n_e}$ Hz, ω is the laser frequency.

The electron number density and plasma temperature obtained at 30 ns delay time at threshold irradiance (~5 GW/cm^2) are $\sim 2\times10^{19}cm^{-3}$ and $\sim 3eV$ for the aspect ratio of 4 cavity. Using the relations $n_e \propto t^{-1.51}$ and $T \propto t^{-1.08}$ [4], the electron number density and plasma temperature at the time of termination of the laser pulse (t = 3 ns) are estimated to be $\sim 6.5\times10^{20}cm^{-3}$ and $\sim 36eV$. The corresponding plasma frequency is $\sim 2.3\times10^{14}Hz$. Since the 266nm laser frequency is $1.13\times10^{15}Hz$, the first case in Eq.

(17) is more suitable. For the threshold irradiance ~5 GW/cm^2 with beam size 50μm, the corresponding laser power is $\sim 9.8\times10^4 W$. The calculated $PT^{5/4}$ is $\sim 8.6\times10^6$, close to the criteria value in Eq.(17).

Due to radiation reflection and plasma confinement effects, plasma shielding causes increased temperatures and electron number densities for laser ablation in a cavity compared to a flat surface. The greater the cavity aspect ratio, the greater the plasma temperature and electron number density [4]. The higher plasma temperature and electron number density in a cavity causes self-focusing of the laser by the plasma, producing higher laser light intensities. Thus phase explosion occurs at a lower laser energy. Therefore, the threshold value decreases for laser ablation in a cavity and the greater the cavity aspect ratio, the smaller the threshold.

4. Summary

The formation of a laser induced plasma inside a cavity was investigated and compared with laser ablation on a flat surface. Plasma temperature and electron number density both in the cavity and on the flat surface change dramatically after the laser beam reaches a threshold irradiance. The threshold irradiances are lower for laser ablation in the cavities than on the flat surface. The greater the cavity aspect ratio, the lower the threshold irradiance. After the irradiance reaches the threshold irradiance, ionization becomes saturated for both the cavity and flat surface. The crater depths were increased approximately by an order of magnitude from the depths below the threshold value. Phase explosion was discussed to explain the large change of both plasma characteristics

and mass removal when irradiance increases beyond a threshold value. Self-focusing of the laser beam could be responsible for the decrease of the threshold value in cavities.

5. Acknowledgments

This research was supported by the U.S. Department of Energy, Office of Basic Energy Sciences, Chemical Sciences Division, under contract No. DE-AC03-76SF00098.

References

[1] M.V. Allmen, A. Blatter, Laser-beam Interactions with Materials – Physical Principles and Applications, 2nd ed (Springer-Verlag, Berlin, 1995).

[2] E. N. Sobol, Phase Transformations and Ablation in Laser-Treated Solids (John Wiley & Sons, New York, 1995).

[3] L. W. Boyd, Laser Processing of Thin Films and Microstructures (Springer-Verlag, New York, 1987).

[4] A.J.G. Mank, P.D. Mason, J. Anal.At.Spectrom. 14, 1143 (1999).

[5] O.V. Borisov, X. Mao, R. E., Russo, Spectrochim. Acta Part B 55, 1693 (2000).

[6] S.M. Eggins, L.P.J. Kinsley, J.M.G. Shelley, Appl.Surf.Sci. 127-129, 278 (1998).

[7] X.Z. Zeng, S.S. Mao, C.Y. Liu, X.L. Mao, R. Greif, R.E. Russo, Spectrochim. Acta Part B, 58, 867 (2003).

[8] J.F. Ready, Effects of High-Power Laser Radiation (Academic, New York, 1971).

[9] M. A. Shannon, Applied Surface Science, 127-129, 218 (1998).

[10] S. H. Jeong, R. Greif, R.E. Russo, J. Appl. Phys. 80, 1996 (1996).

[11] H.C. Liu, X.L. Mao, J.H. Yoo, R.E. Russo, Spectrochim. Acta Part B 54, 1607 (1999).

[12] J.H. Yoo, S.H. Jeong, R. Greif, R.E. Russo, J. Appl. Phys. 88, 1638 (2000).

[13] G.J. Bastiaans, R.A. Mangold, Spectrochim.Acta, Part B 40B, 885 (1985).

[14] H.R. Griem, Principles of Plasma Spectroscopy (Cambridge University Press, 1997).

[15] Atomic Spectra Databases. Version 2.0. National Institute of Standards and Technology (NIST), USA, 1999. (http://www.nist.gov).

[16] S. Tamaki, T. Kuroda, Spectrochimica Acta, 42B, 1105 (1987).

[17] A.A. Pupyshev, E.V. Semenova, Spectrochim. Acta Part B 56, 2397 (2001).

[18] H.R. Griem, Spectral Line Broadening by Plasmas (Academic, New York, 1974).

[19] G. Befeki, Principles of laser plasmas (Wiley Interscience, New York, 1976).

[20] P.J. Wolf, J.Appl.Phys. 72, 1280 (1992).

[21] R.W.P. McWhirter, in: R.H. Huddlestone and S.L. Leonard (Eds.), Plasma Diagnostic Techniques (Academic, New York, 1965).

[22] C.R. Phipps, R.W. Dreyfus, in: A. Vertes, R. Gijbels, F. Adams (Eds.), Laser Ionization Mass Analysis (John Wiley & Son, New York, 1993).

[23] R.K. Singh, J. Narayan, Phys.Rev. B 41, 8843 (1990).

[24] S.S. Harilal, C.V. Bindhu, Riju C. Issac, V.P.N. Nampoori, and C.P.G. Vallabhan, J.Appl.Phys. 82 (5), 2140 (1997).

[25] A. Miotello and R. Kelly, Appl. Phys. Lett. 67, 3535 (1995).

[26] R. Kelly and A. Miotello, Appl. Surf. Sci. 96-98, 205 (1996).

[27] H. Hora, Plasma at High Temperature and Density- Applications and Implications of Laser-Plasma Interaction (Springer-Verlag, New York, 1991).

Figure Captions

Fig. 1. Si(I) 288.16 nm spectral line and continuum emission at time of 30 ns, distance of 1 mm and irradiance of 15 GW/cm^2. Compare flat surface and cavity (Diameter 250 micron, depth 500 micron) ablation results. Bold lines are Lorentzian fitting curves.

Fig. 2. (a) Electron number density and (b) plasma temperature vs. irradiance. Compare flat surface and two cavity (Diameter 130 micron, depth 500 micron, aspect ratio 4; Diameter 250 micron, depth 500 micron, aspect ratio 2) ablation results at time of 30 ns and distance of 1mm. Sample was fused silica.

Fig. 3. Electron number density and plasma temperature vs. distance from surface at below and above threshold irradiances. Compare (a, b) flat surface and (c, d) cavity (Diameter 130 micron, depth 500 micron) ablation results at time of 30 ns.

Fig. 4. Silicon ionization efficiency vs. irradiance. Compare (a) flat surface and two cavity ((b) Diameter 130 micron, depth 500 micron, aspect ratio 4; (c) Diameter 250 micron, depth 500 micron, aspect ratio 2) ablation results at time of 30 ns and distance of 1 mm.

Fig. 5. Inverse bremsstrahlung absorption coefficient at time of 30 ns and distance of 1 mm vs. irradiance.

Fig. 6. Crater depth resulting from single pulse laser ablation on fused silica vs. irradiance.

Fig. 7. Images obtained by laser shadowgraphy for laser irradiances of (a) 21 GW/cm^2 and (b) 18 GW/cm^2 at time of 2 μs.

Table I. Coefficients for partition functions of silicon atom, singly-charged and doubly-charged silicon ions (Eq. 4)

	a	b	c	d	e	f
Si	14.534	21.9	-58.135	41	-7.8237	0.5011
Si^{+}	4.9632	1.8184	-1.445	0.52732	-0.00596	-0.0036
Si^{2+}	1.3178	-0.61576	0.33364	-0.02366	-0.00367	0.00122

Table II. The parameters used for plasma temperature and electron number density calculations

$A_{21}(10^8 s^{-1})$	g_2	$E_2(eV)$	$E_i(eV)$	ξ	G	$W(nm)$	A	$C_r(sK)$
1.9	3	5.028	8.151	1.4	1	0.848×10^{-3}	0.027	2.005×10^{-5}

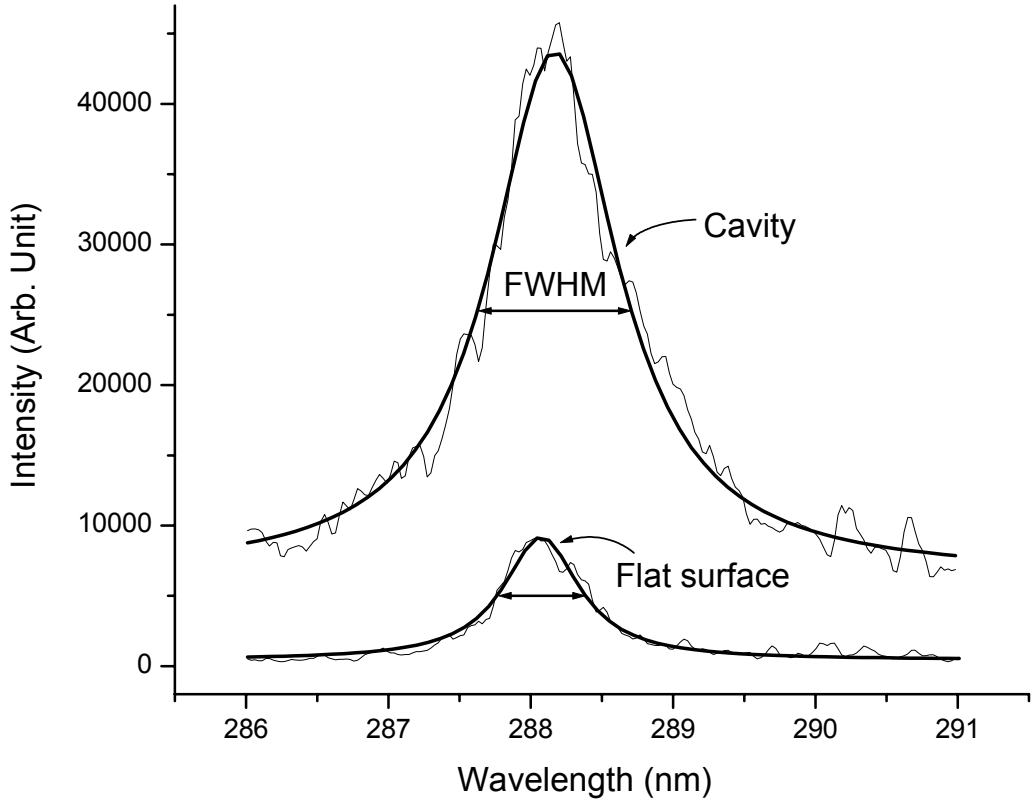
Intensity (Arb. Unit)
40000
30000
20000
10000
0
Cavity
FWHM
Flat surface
286
287
288
289
290
291
Wavelength (nm)

Fig. 1

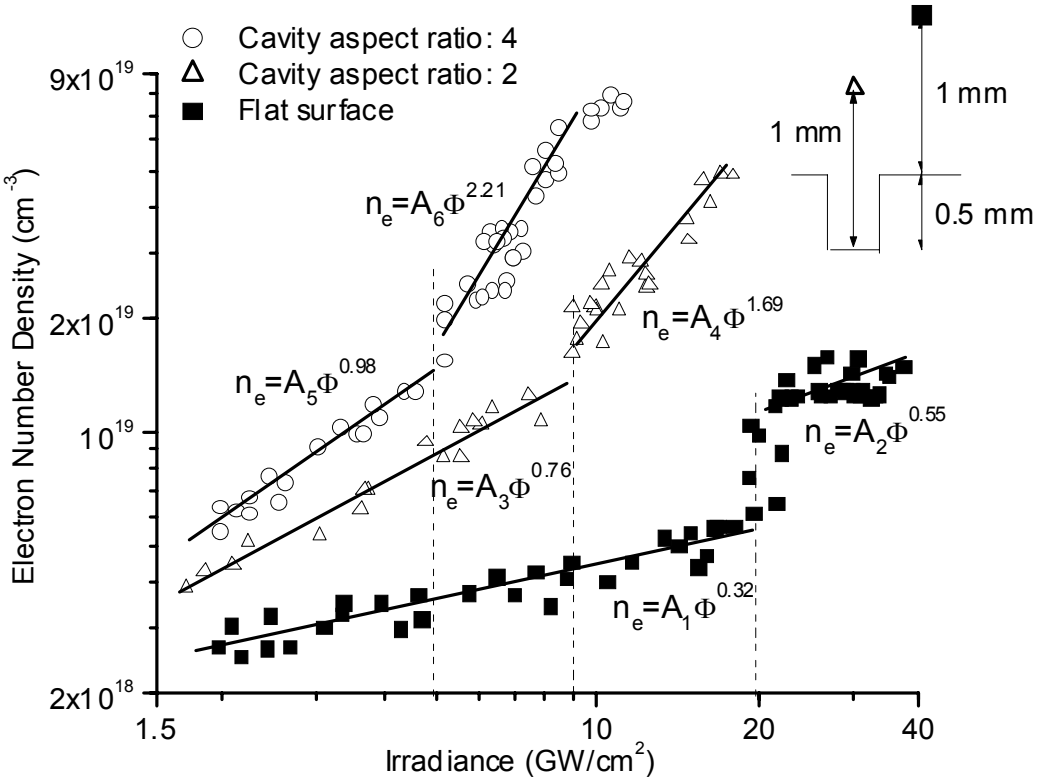
Cavity aspect ratio: 4
Cavity aspect ratio: 2
Flat surface
9x10^19
2x10^19
10^19
2x10^18
Electron Number Density (cm^-3)
n_e=A_6Φ^2.21
n_e=A_4Φ^1.69
n_e=A_5Φ^0.98
n_e=A_3Φ^0.76
n_e=A_2Φ^0.55
n_e=A_1Φ^0.32
1 mm
1 mm
0.5 mm
1.5
10
20
40
Irradiance (GW/cm^2)

(a)

Fig. 2a

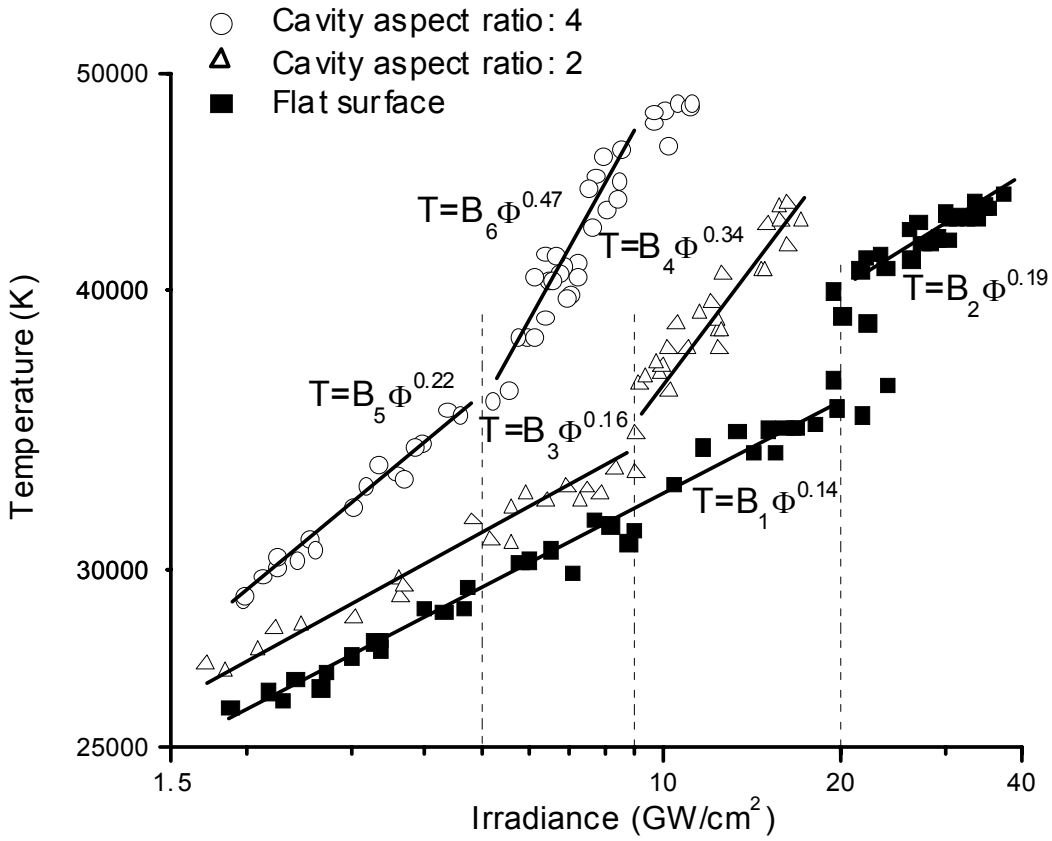
Cavity aspect ratio: 4
Cavity aspect ratio: 2
Flat surface
T=B6Φ0.47
T=B4Φ0.34
T=B2Φ0.19
T=B5Φ0.22
T=B3Φ0.16
T=B1Φ0.14
Temperature (K)
50000
40000
30000
25000
1.5
10
20
40
Irradiance (GW/cm2)

(b)

Fig. 2b

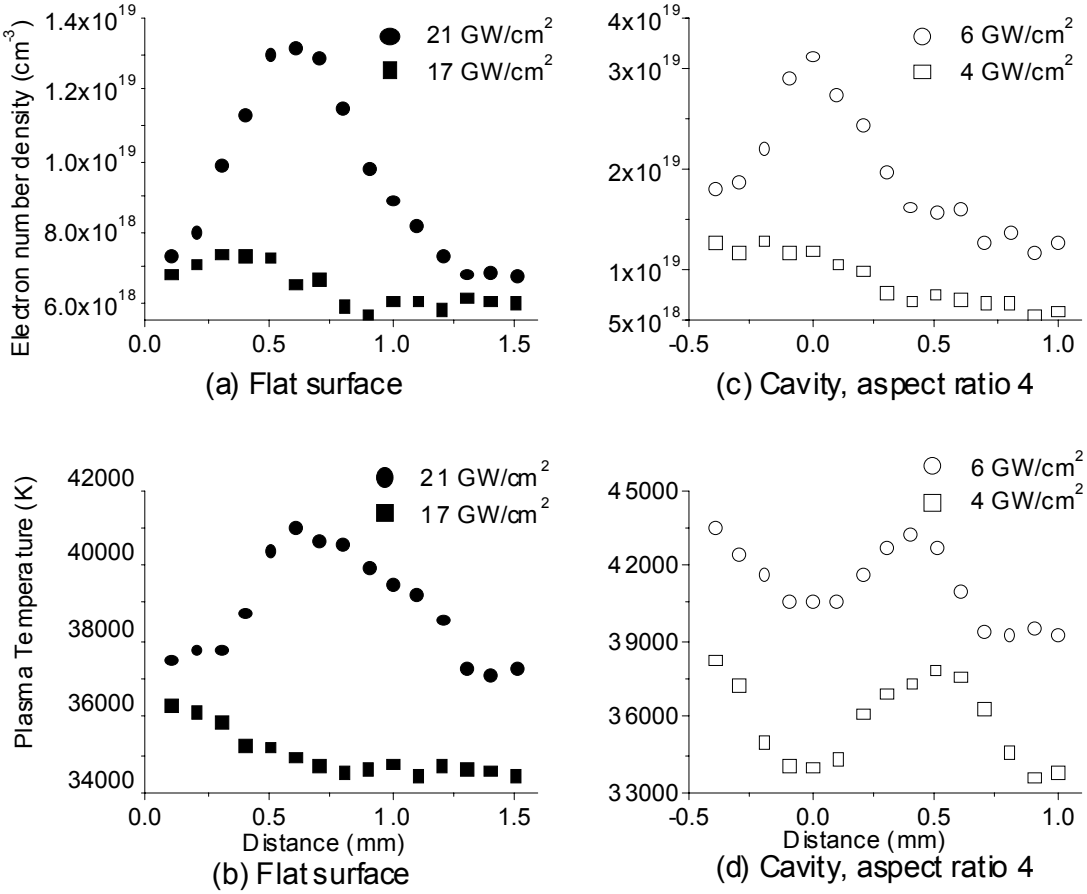
Electron number density (cm^{-3})
1.4x10^{19}
1.2x10^{19}
1.0x10^{19}
8.0x10^{18}
6.0x10^{18}
0.0
0.5
1.0
1.5
21 GW/cm^2
17 GW/cm^2
(a) Flat surface
4x10^{19}
3x10^{19}
2x10^{19}
1x10^{19}
5x10^{18}
-0.5
0.0
0.5
1.0
6 GW/cm^2
4 GW/cm^2
(c) Cavity, aspect ratio 4
Plasma Temperature (K)
42000
40000
38000
36000
34000
0.0
0.5
1.0
1.5
Distance (mm)
21 GW/cm^2
17 GW/cm^2
(b) Flat surface
45000
42000
39000
36000
33000
-0.5
0.0
0.5
1.0
Distance (mm)
6 GW/cm^2
4 GW/cm^2
(d) Cavity, aspect ratio 4

Fig. 3

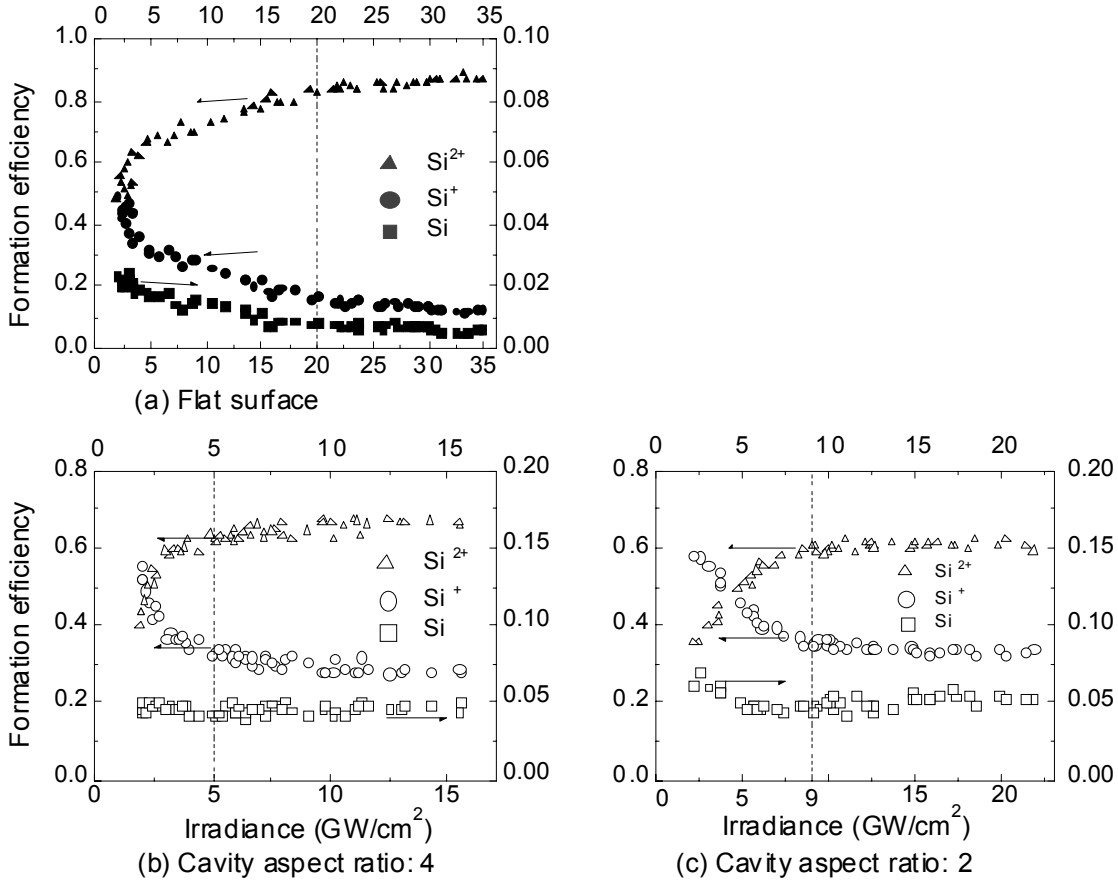
Formation efficiency
Si2+
Si+
Si
(a) Flat surface
Formation efficiency
Irradiance (GW/cm2)
(b) Cavity aspect ratio: 4
(c) Cavity aspect ratio: 2

Fig. 4

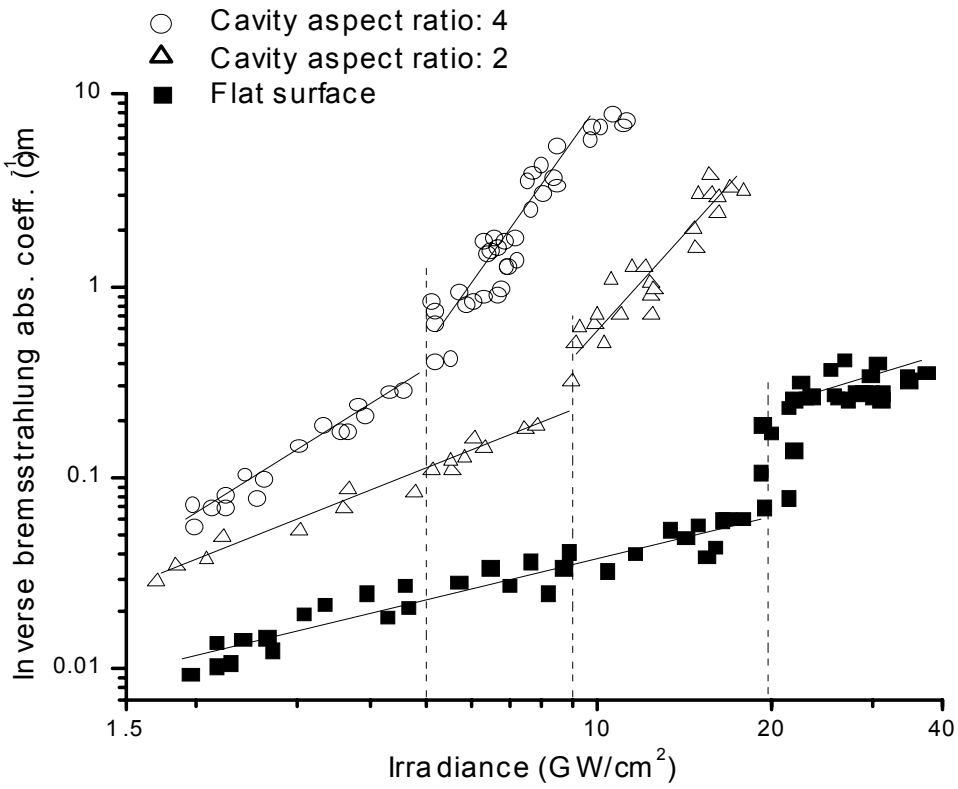
Cavity aspect ratio: 4
Cavity aspect ratio: 2
Flat surface
Inverse bremsstrahlung abs. coeff. (cm-1)
10
1
0.1
0.01
1.5
10
20
40
Irradiance (GW/cm2)

Fig. 5

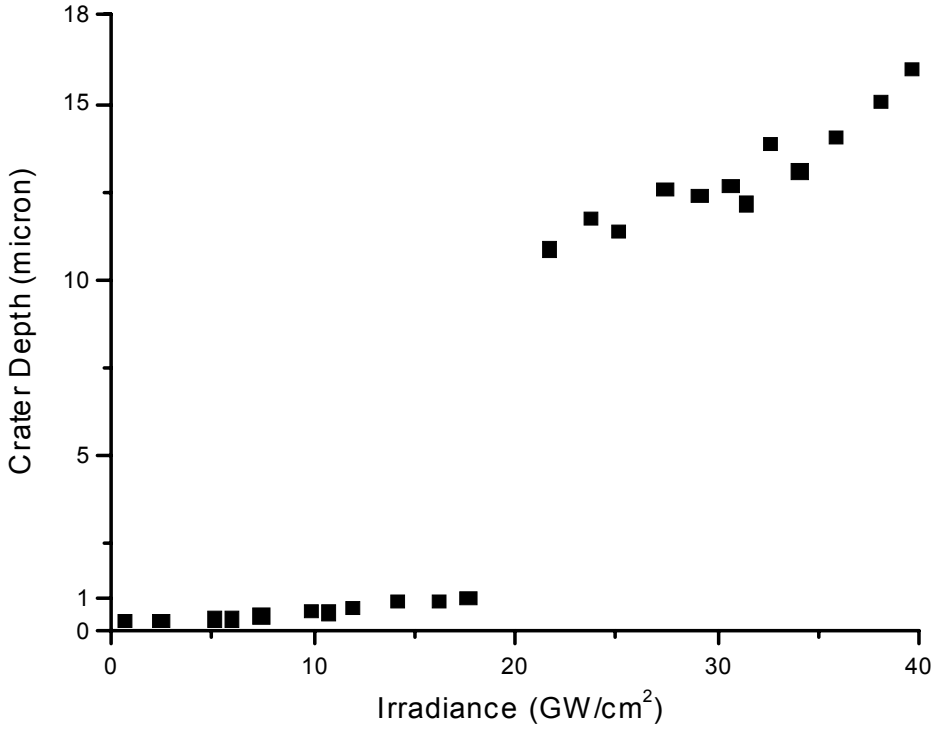
Crater Depth (micron)
18
15
10
5
1
0
0
10
20
30
40
Irradiance (GW/cm^2)

Fig. 6

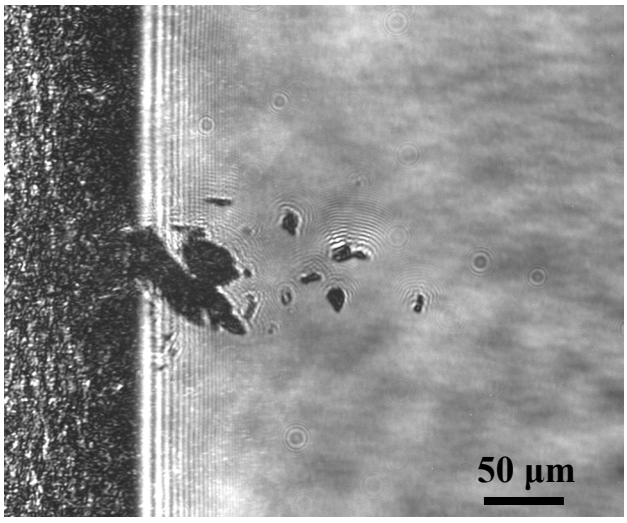

(a)

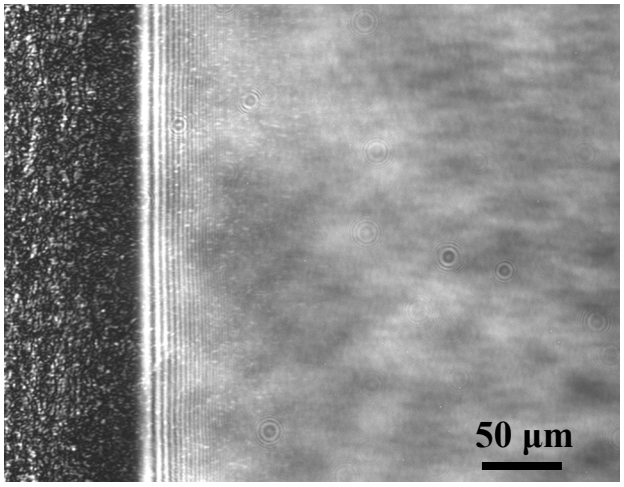

(b)

Fig. 7